Parametric analysis and machine learning-based parametric modeling of wire laser metal deposition induced porosity

Tanguy Loreau[1] · **Victor Champaney**[1] · **Nicolas Hascoet**[1] · **Jon Lambarri**[2] · **Mikel Madarieta**[2] · **Iker Garmendia**[2] · **Francisco Chinesta**[1]

Abstract

Additive manufacturing is an appealing solution to produce geometrically complex parts, difficult to manufacture using traditional technologies. The extreme process conditions, in particular the high temperature, complex interactions and couplings, rich metallurgical transformations and combinatorial deposition trajectories, induce numerous process defects and in particular porosity. Simulating numerically porosity appearance remains extremely complex because of the multiple physics induced by the laser-material interaction, the multiple space and time scales, with a strong impact on the simulation efficiency and performances. Moreover, when analyzing parts build-up by using the wire laser metal deposition —wLMD— technology it can be noticed a significant variability in the porosity size and distribution even when process parameters remain unchanged. For these reasons the present paper aims at proposing an alternative modeling approach based on the use of neural networks to express the porosity as a function of different process parameters that will be extracted from the process analysis.

Introduction

Additive manufacturing –AM– with all its variants is widely used for manufacturing complex parts and more

✉ Francisco Chinesta
   francisco.chinesta@ensam.eu

   Tanguy Loreau
   tanguy.loreau@ensam.eu

   Victor Champaney
   victor.champaney@ensam.eu

   Nicolas Hascoet
   nicolas.hascoet@ensam.eu

   Jon Lambarri
   jon.lambarri@tekniker.es

[1] PIMM Laboratory, ESI Group Chair, Arts et Métiers Institute of Technology, CNRS, Cnam, HESAM Université, 151 boulevard de l'Hôpital, 75013, Paris, France

[2] TEKNIKER, Parke Teknologikoa, Iñaki Goenaga, 5, 20600, Eibar, Gipuzkoa, Spain

particularly, for enhancing materials and structures by integrating many functionalities. Architectured materials and metamaterials, empowering structures, are nowadays present in all the domains of science and engineering.

However, AM processes involve nowadays many challenges related to the modeling, simulation and process control. These difficulties come from the multiple and coupled physical phenomena, highly localized in space and time, affecting different scales, from the one of the metallurgy and porosity, to the one of the part in which residual stresses induce the part distortion.

The resulting structural performances are strongly dependent on the process parameters, that affect the local properties that as just mentioned affect the global scale. Between the local scale (at which laser and material interact) and the one of the part, another scale is of major relevance, the one of the deposition trajectory that links the local and the global scales, and that constitutes a real challenge from the computational point of view, not only because of the fact that simulating a printing operation is very expensive (due to the big difference between the local scale and the characteristic length of the printing trajectory). The main difficulty remains expressing the final properties

as a function of the processing parameters. Parametrizing trajectories remains nowadays an open issue.

Thus, structural distortion becomes a consequence of the induced residual stresses and has an impact on structural tolerances. Metallurgy, strongly dependent on the local thermal history, affects the mechanical properties of the formed part. Local defects, as porosity, have major consequences on the mechanical performances, in particular on fatigue [1].

Even if valuable modeling approaches exist in what concerns the evaluation of the induced thermal history and the residual stresses induced in the part, the modeling of defects appearance needs a fine multi-physics approach able to address the numerous coupled and localized mechanisms: laser-matter interaction, phase transformation, induced free surface flows involving surface tension, heat transfer (involving convection, diffusion and radiation), thermo-mechanical couplings, inelastic solid behaviors, ...

Moreover, from an experimental point of view, the defects appearance cannot be predicted in a deterministic way from the local process parameters (the ones at the point where the defect appears), certainly due to the fact that the smaller scales exhibiting an inherent stochasticity, unresolved by the models, have an impact on the defects appearance. For this reason, a statistical analysis is retained, trying to express the average of the porosity with the average of the process parameters, within a representative volume enabling such a statistical analysis.

Artificial intelligence, and more particularly machine learning techniques, able to produce accurate regressions as soon as an enough amount of data is available, constitute an appealing route for correlating the defects distribution with the process parameters.

Several works exist addressing defects in AM. Some of them concern experimental approaches, others are based on mechanistic models and finally some other follow the route based on data-driven approaches.

In particular, [2] provides a full review about additive manufacturing and the challenges that it implies, both technical, environmental and economical. In [3, 4] authors give an overview on Direct Laser Deposition –DLD– techniques. A special concern is given on process parameters, physical phenomena, high fidelity modeling, defects and their sources and the resulting mechanical properties of the printed part. Other reviews now addressing Wire and Arc Additive Manufacturing –WAAM– are addressed in [5, 6]. One of the main challenges in additive manufacturing remains of predicting the mechanical properties of the printed parts.

Therefore, some experimental studies focus on the characterization of micro and meso structures of printed parts and, in particular pores, that originate cracks in fatigue [7–10]. For Ti6Al4V alloy, also the material used in the present study, results in [11] argue that porosity increases with injected mass flow rate and decreases by reducing overlapping distance while [12] concludes that increasing scanning speed and laser power can be beneficial.

In addition, in order to predict the quality of printed parts, some studies address the finite element modeling of AM processes. Most of them focus on the final geometry of the printed parts, affected by the installed residual stresses, while minimizing porosity with well chosen process parameters [13, 14], porosity that many times is assumed homogeneously distributed in the whole part [15, 16]. High fidelity models to predict porosity in printed parts remain an active field of research. Thus, [17] predicts porosity in powder bed process and [18] predicts the most probable locations of porosity in the printed part in the case of LMD processes. Another physics-based analytical model to predict lack-of-fusion porosity can be found in [19] for a powder-bed based AM process.The approach considers a moving heat source solution. Parallel hatching is studied, with overlapping and layer thickness as the input parameters. More complex multi-physics models, such as [20–22] rely on finite volume methods (FVM) with interface tracking and complex laser - matter interaction.

To overcome the computational cost induced by the intense physical mechanisms couplings (laser-matter interaction, phase transformation,...), machine learning can represent a great opportunity [23]. Garg et al. [24] proposes a data-driven model to predict the total amount of porosity in a Selective Laser Manufactured –SLM– part. For LMD processes, [25] develops an in-situ monitoring based on the employ of artificial intelligence that predicts online the apparition of porosity. [26] uses a similar approach to predict porosity with a database of images of printed surfaces, a physics-driven model and a deep-learning convolutional neural network.

The present paper aims at proposing an alternative modeling approach based on the use of neural networks to express the porosity as a function of different process parameters that will be extracted from the process analysis.

Finer approaches will be considered in future works in progress where the Neural Networks –NN– based regressions will include also data coming from simulations, as for example the local temperature history and its time and space gradients, as well as the associated stress fields.

Experiments and collected data

A set of experiments, using wLMD technology, was carried out to evaluate the effect of process parameters and trajectory settings on defectology, namely lack of fusion and porosity. Aeronautical grade Ti6Al4V alloy was used both for the substrate and deposited material. The filling

strategy consisted on zig-zag tracks, with 90° alternating directions in consecutive layers, plus a contour at the perimeter. A design of experiments (DoE) consisting of 18 different combinations was proposed, using a simple wall-like geometry, 5 of which failed to provide the required data. The remaining 13 parts were examined for defects by using x-ray computed tomography (CT) scans, by means of a 450kV system, providing an approximate spatial resolution of 100μm. The process conditions of the parts that were successfully printed are reported in Table 1.

Regarding the experimental set-up, a fibre laser generator (active media: Ytterbium) with a maximum power of 4 kW was used as the energy source. The laser beam was guided to the interaction area by a 600 μm diameter optical fibre, coupled to a three-beam coaxial head, attached in turn to a 6-axis robot. To avoid oxidation during the Ti-6Al-4V deposition process, a controlled atmosphere chamber was used, where oxygen is evacuated by injecting pressurized argon.

The tool centre point (TCP) position, as evaluated by the robot controller, was logged during the deposition, alongside a binary parameter to register whether the laser was on or off. CT scans were then extracted and referenced to the same system as the robot. Processed results include void volume, centroid coordinates, and projected size alongside the three spatial coordinates, as illustrated in Fig. 1.

Data analysis

Data processing

The present study considers 13 manufactured parts. Each of them was processed by considering a different deposition
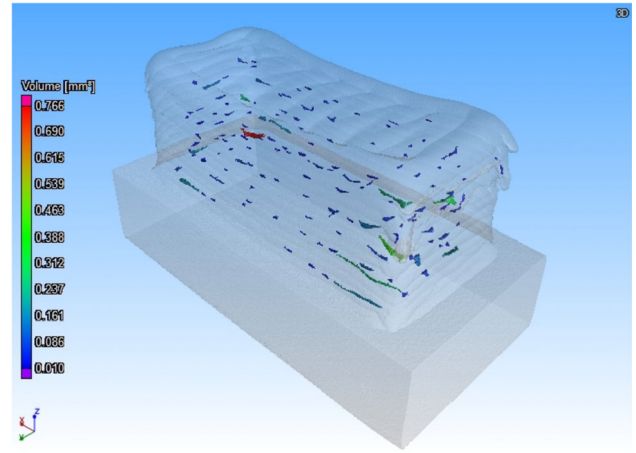

Fig. 1 Tomography results showing void volume and location

trajectory, that will induce a variety of data-points with different states (local velocity, acceleration, ...) to be correlated with the local measured fraction of porosity, the last obtained as previously indicated by using tomography scanning. Among the other process parameters reported in Table 1 only the laser power will be introduced later in the proposed modeling approach. In the proposed modeling approach, the layer thickness was considered instead of the injected mass, the extracted local velocities from the trajectory data instead of the robot speed, and the density of turns instead of the overlapping distances because of the fact that the porosity in the internal regions of the domain seems quite insensible to that overlapping distance.

Pores will be described by using their bounding boxes, and more concretely as sketched in Fig. 2, the boxes center and size.

Concerning the processing data, it consists of:

– Laser activation state at each time: On/Off;

Table 1 DoE reporting the process conditions

Test reference	Injected mass (g/min)	Laser power (W)	Robot speed (mm/min)	Overlapping distance (mm)
1	9	1700	20	2,5
2	11	1950	20	1,8
3	13	2450	20	2,0
4	7	1200	30	1,3
5	9	1500	30	2,9
6	9	1800	30	1,2
7	11	2100	30	1,5
8	13	2400	30	1,6
9	15	2700	30	1,8
10	15	3000	30	2,0
11	7	1500	40	2,8
12	11	2100	40	2,4
13	13	2400	40	2,5

Fig. 2 Representing a pore from its bounding box
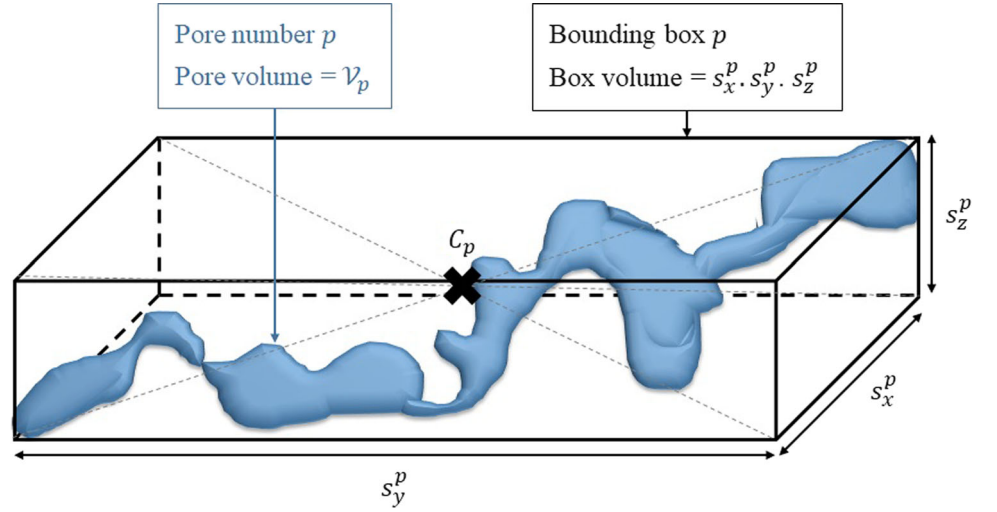
- Laser coordinates at each time t_i, $i = 1, ..., \mathcal{T}$: $X(t_i) = [x(t_i), y(t_i), z(t_i)]$;
- Number of printed layers.

Concerning the porosity, it is given by a set of $\mathcal{P}$ bounding boxes, each characterized by the following information:

- Geometrical center: $C_p = [x_p, y_p, z_p]$, $p = 1, ..., \mathcal{P}$;
- Volume of the pore: $\mathcal{V}_p$, $p = 1, ..., \mathcal{P}$;
- Box size in the three coordinate axes: $\{s_x^p, s_y^p, s_z^p\}$, $p = 1, ..., \mathcal{P}$.

The knowledge of the laser position at each time step, allowed calculating the velocity at each time, making use of a standard finite difference scheme. The computed velocities were then filtered by averaging them in a moving window covering a number of time steps (20 in the cases here treated) and moving with the laser. Figure 3 compares the computed and averaged (filtered) velocities, the last exhibiting a much smaller fluctuation.

The parts will be decomposed in a number of boxes where averages of the different parameters will be calculated to be then correlated with the volume fraction of porosity inside those boxes. More details on the construction of these computational boxes will be given later. If N velocities are known inside a computational box, noted by $\overrightarrow{v}^i = [v_X^i, v_Y^i, v_Z^i]$, $i = 1, ..., N$, the planar averaged velocity reads
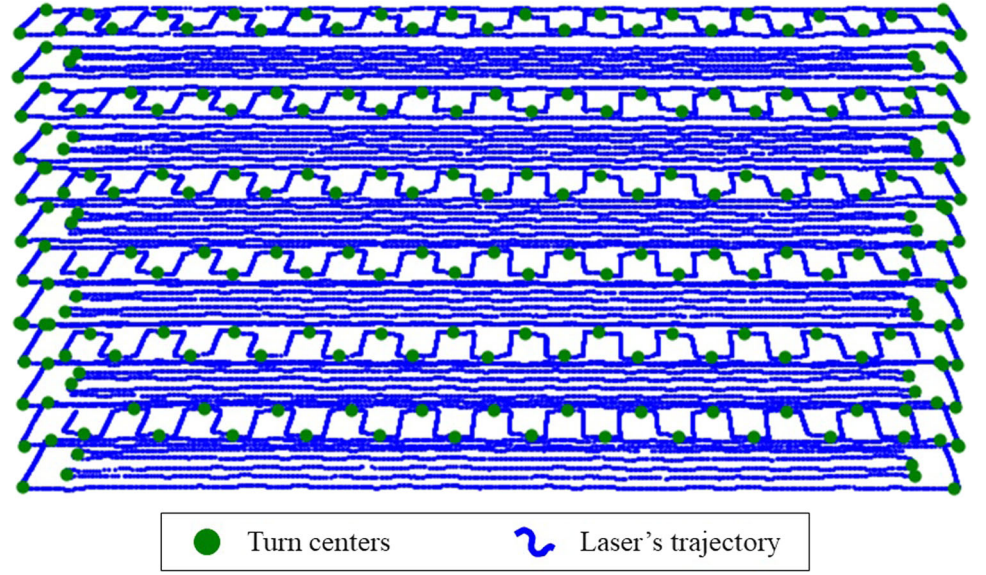
$$\overline{V}_{XY} = \frac{1}{N} \sum_{i=1}^{N} \left\| v_X^i \overrightarrow{x} + v_Y^i \overrightarrow{y} \right\|, \tag{1}$$

Fig. 3 Computed versus averaged velocities
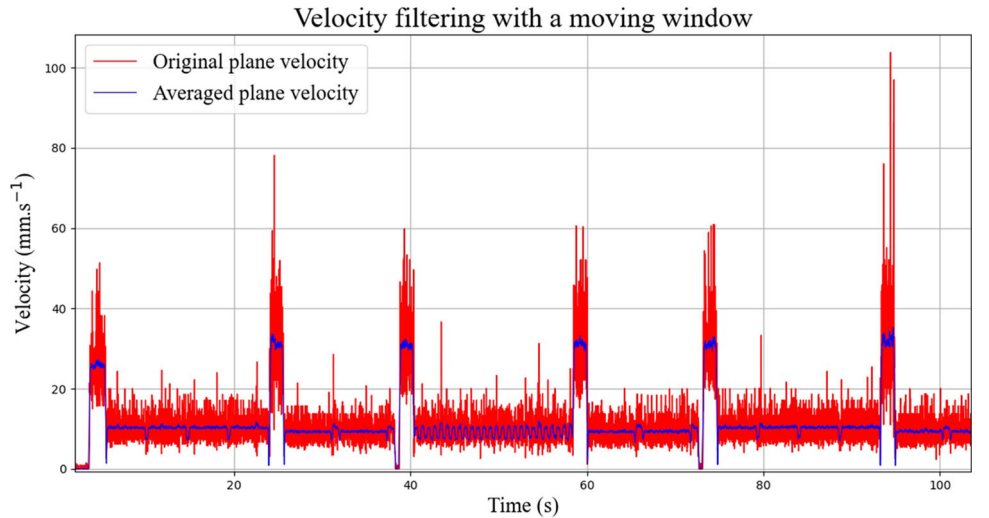
**Fig. 4** Turns (green dots) extracted from the trajectory data (blue line)

| ● Turn centers | 〰 Laser's trajectory |

whereas the averaged directional velocity, along the direction defined by the unit vector $\overrightarrow{u}$ reads

$$\overline{V}_u = \frac{1}{N} \sum_{i=1}^{N} \overrightarrow{v}^i \cdot \overrightarrow{u}. \tag{2}$$

The trajectories could also affect the porosity, and more particularly the locations where the deposition direction changes. Thus, the number of trajectory turns occurring in a computational box could exhibit a correlation with the observed porosity. An appropriate algorithm was implemented for identifying the changes in trajectory direction, based on the variation of the tangent vector calculated along the laser trajectory. Figure 4 depicts the identified turns. As it can be seen in this figure successive layers have a different printing strategy, implying a different location of the trajectory turns.

Concerning porosities previously discussed, considering that a pore belongs to the computational box in which the pore bounding box center is located, represents a too crude approximation, as depicted in Fig. 5.
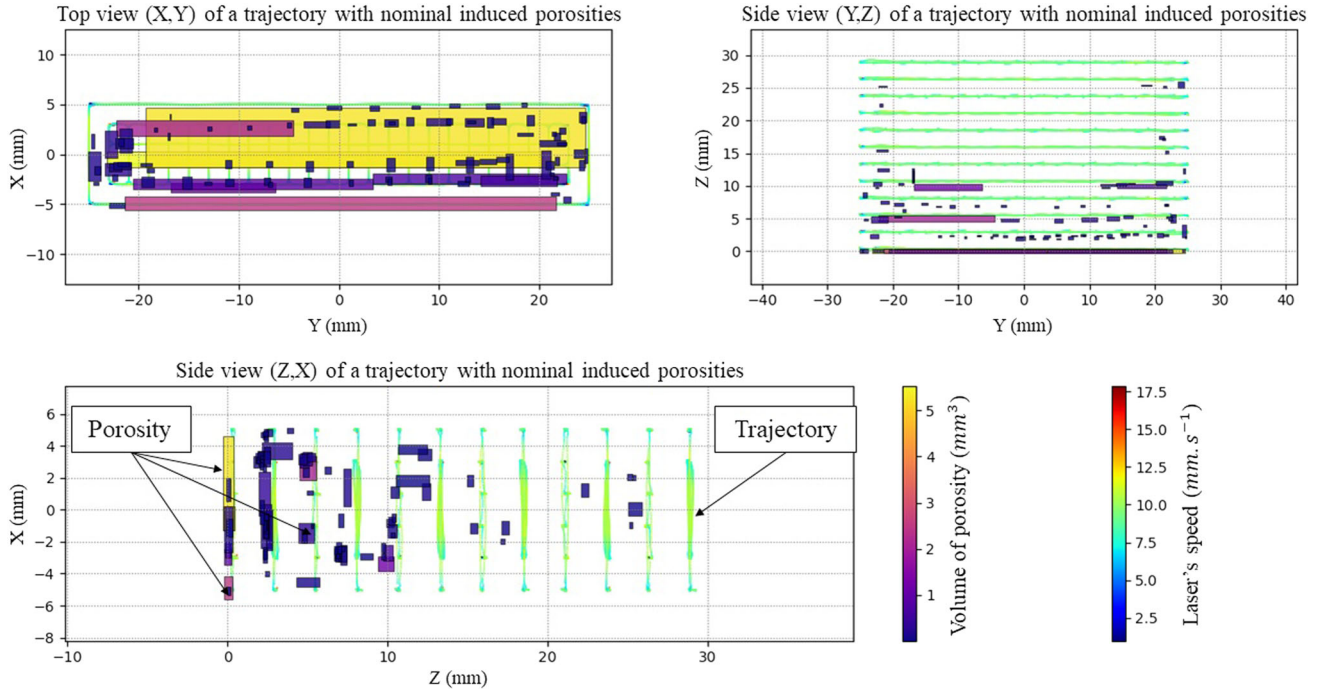
Fig. 5 Porosity bounding boxes
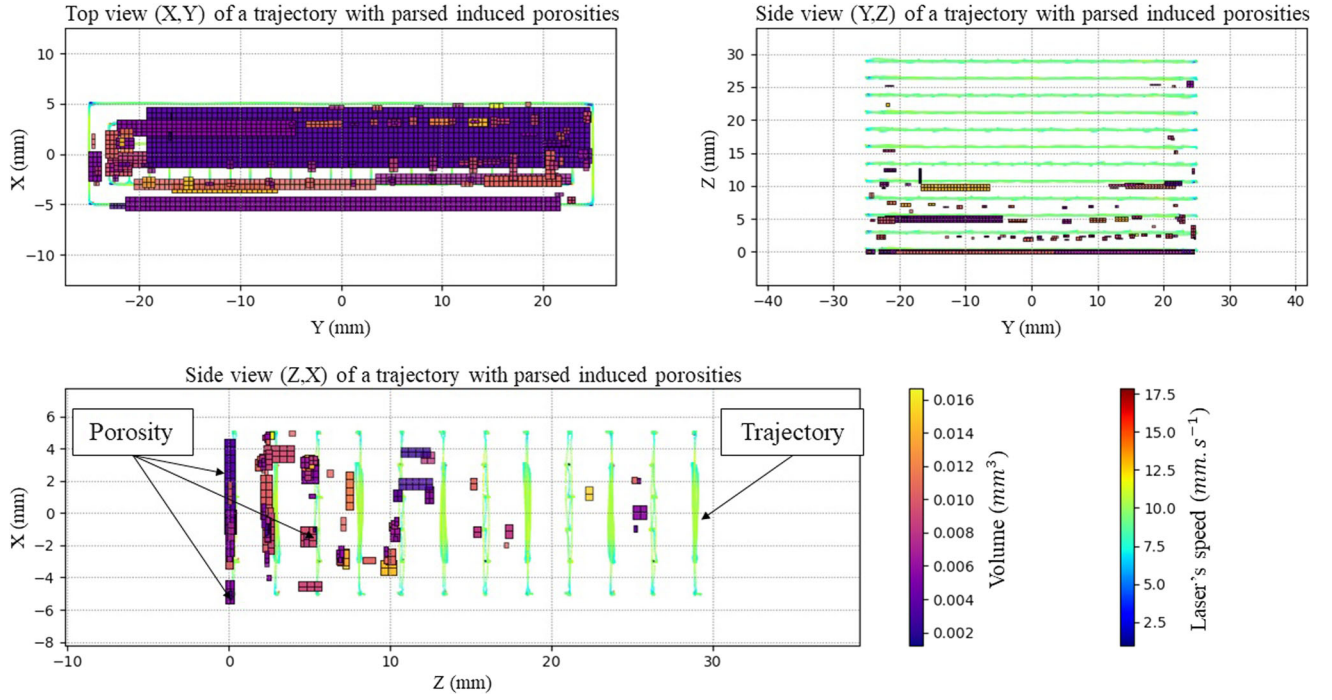
Fig. 6 Refined porosity bounding boxes

In order to refine the porosity description, the bounding box representing a pore is decomposed in a number of smaller boxes of a given size (able to represent the smaller porosity), in our case the size of these sub-boxes are $0.5 \times 0.5 \times 0.5$ mm^3). The new porosity description is illustrated in Fig. 6.

To correlate process parameters with the induced porosity, we must define, as previously introduced, a computational box (representative volume) large enough for computing the average value of the parameters inside the box (velocities, trajectory turns, ...), but not too large, to ensure that these averages are a right statistical representation of the quantities into the box.

In the considered cases, the domain was decomposed $1 \times 5 \times 4$ boxes (referring respectively to the coordinate axes x, y and z), as depicted in Fig. 7. As can be seen in

Fig. 7 Computational boxes covering a printed part
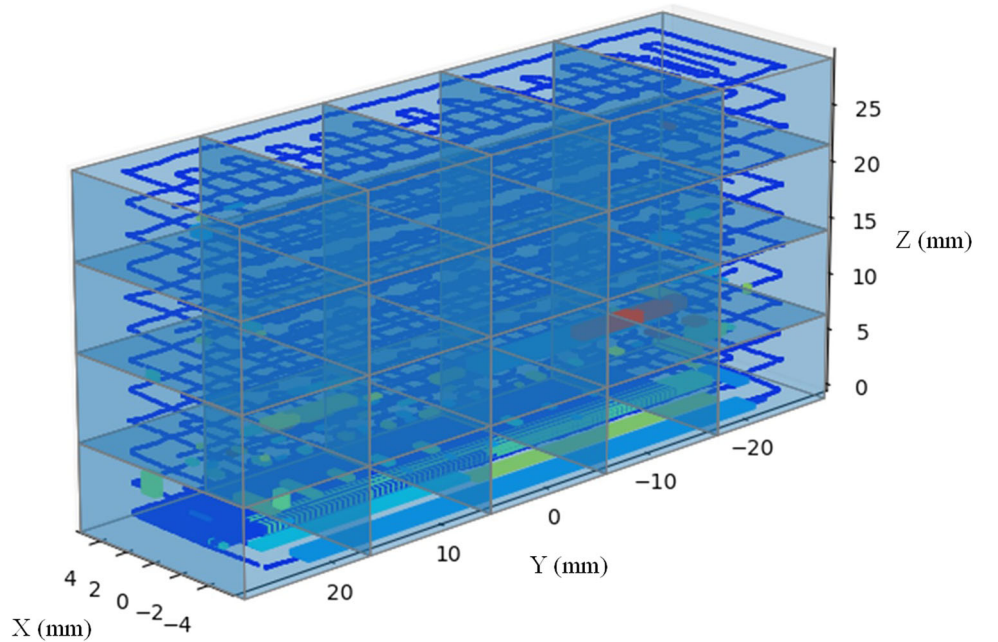
this image, each box concerns many layers, and then many different trajectories (along the x-direction and along the y-direction).

Proposal and analysis of parameters affecting the local porosity

Different parameters are expected to have a potential impact on the observed porosity. This porosity, as described before, is observed preferentially in the periphery of the part (lateral surfaces) as well as in the neighborhood of the interface between the part and the substrate.

Among the potential parameters expected to affect the porosity, the first candidates are: the velocity along the x and y directions, the magnitude of the average planar velocity, the laser power, the box index that serves to locate the box (internal or located on the part periphery), the box location with respect to the substrate, the layer thickness and the density of trajectory turns (number of turns divided by the box volume).

With the average of all these variables calculated in each computational box, the available data (20 boxes for each of the 13 formed parts) is used to evaluate the correlation between the fraction of porosity (volume of pores in each computational box divided by the box volume).

In the representations that follow, that aims at comparing the tendencies to the existing technical expertise, the x-axis will report the considered parameter whereas the y-axis will report the volume fraction of porosity. In some cases, the zero value of the considered parameter will be emphasized

by adding a vertical red line at the zero value of the considered parameter (in particular when considering the averaged velocities). The diagrams will include the medians (horizontal red segments), the lower and upper quartiles (the representation boxes), the whiskers extend to the last value lower than $2.5Q_3 - 1.5Q_1$ and greater than $2.5Q_1 - 1.5Q_3$, where Q_1 and Q_3 are respectively the lower and the upper quartiles, as well as the outlier data (points outside). The total number of pores (in the refined representation discussed before) is also indicated in the top of the figures.

1. **Average velocity in the x-direction.**

   Figure 8 represents the porosity versus the average velocity along the x-direction. If we consider the five computational boxes along the y-direction, when printing along the x-direction the average velocity in the x-direction almost vanishes, with an amount of porosity located at the minimum and maximum values of the x-coordinate, locations related to the trajectory turns. Thus, some amount of porosity is expected when the average velocity in the x-direction vanishes. Then, for the layers where printing occurs along the y-direction, the average velocity in the x-direction is expected vanishing in the internal boxes. However, in the ones located on the border (minimum and maximum values of the y-coordinate) the average velocity in the x-direction does not vanish due to the turns, as illustrated in Fig. 9, and consequently some amount of porosity is also expected for positive and negative
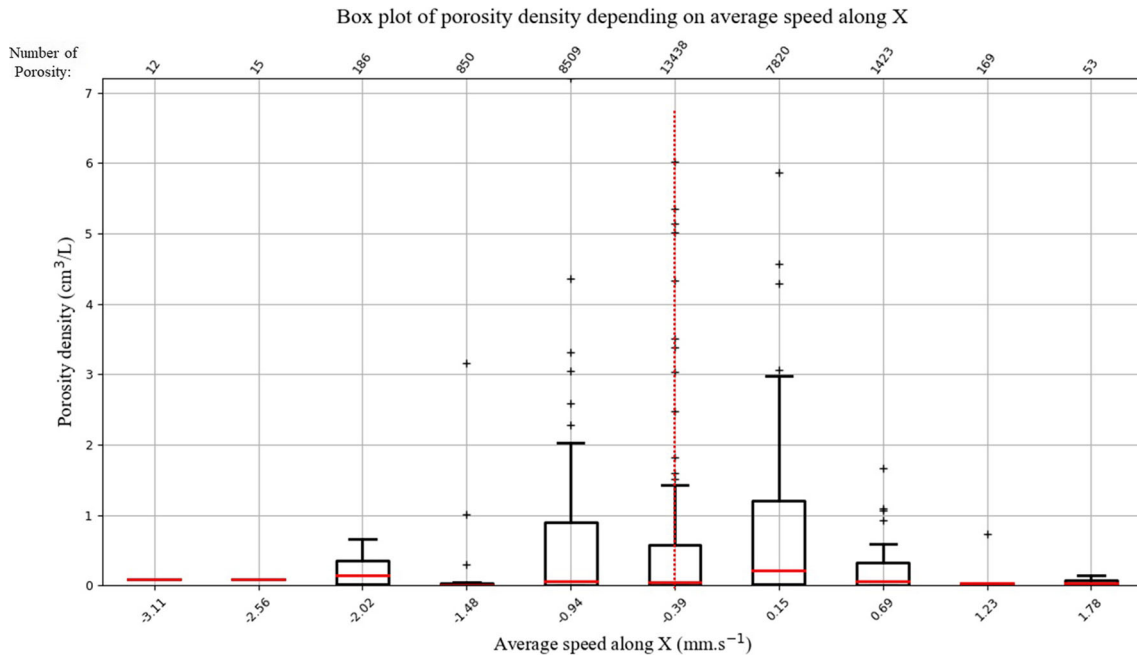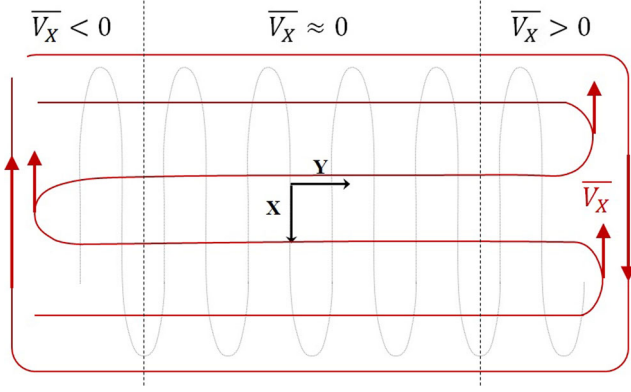

Fig. 8 Porosity versus averaged velocity along the x-direction

Fig. 9 On the distribution of the averaged velocity along the x-direction

averaged velocities in the x-direction, distributed non symmetrically as illustrated in Fig. 9.

2. **Average velocity in the y-direction.**

The same rationale applies now when addressing the average velocity in the y-direction. In this case, when printing in the y-direction, the averaged velocity along the y-direction vanishes, and some amount of porosity is expected localizing around the trajectory turns. Then, when trajectories follow the x-direction, a significant velocity along the y-direction is noticed at the trajectory turns, as sketched in Fig. 10. Thus, in the present case the maximum velocity is expected at non-zero values of

the averaged velocity along the y-direction (in a non-symmetrical way), expectation that is confirmed by the available data represented in Fig. 11.

3. **Average planar velocity.**

The previous discussions confirm the fact that the maximum porosity is expected occurring at the places where the velocity norm vanishes, that corresponds with the locations at which the laser turns. This expectation is confirmed when representing the porosity versus the average planar velocity, as reported in Fig. 12.

4. **Box index referring to its location along the y-direction.**

Figure 13 reports the value of the porosity for the different indexes, 1 to 5, identifying the five locations of the computational boxes along the y-direction. As it can be noticed, and as was expected, the ones located at the borders, the first and fifth, exhibit the higher porosity with respect to the central ones. This fact motivates replacing the boxes index by a new index indicating the relative position of the box, taking the value one for the boxes on the domain edges (first and fifth), two for the intermediate ones (second and fourth) and one for those located in the center. This new index will be noted by `typ`, and the new representation of the porosity with respect to this new parameter is presented in Fig. 14.

5. **Box location along the z-direction.**

It was observed that porosity locates on the neighborhood of the domain boundary, as well as in

Fig. 10 Averaged velocity along the y-direction when: (a) Printing along the y-direction; and (b) Printing along the x-direction
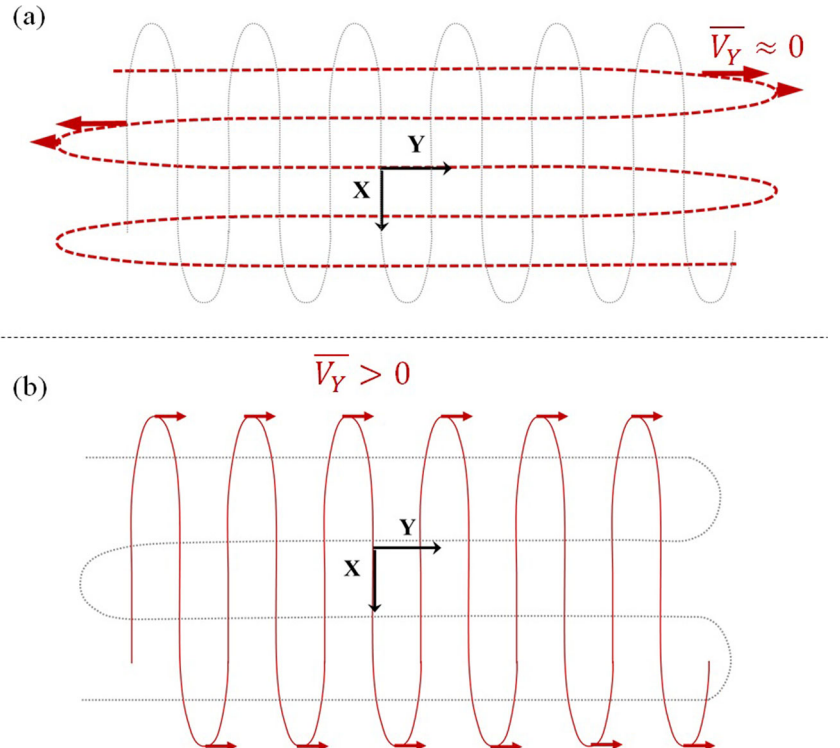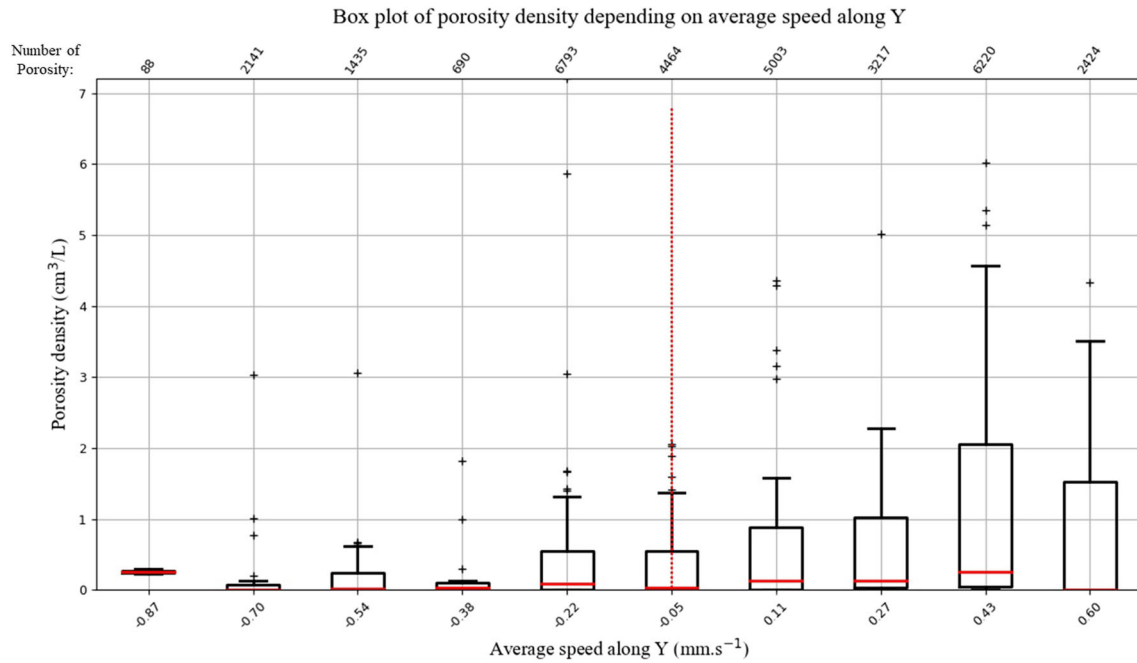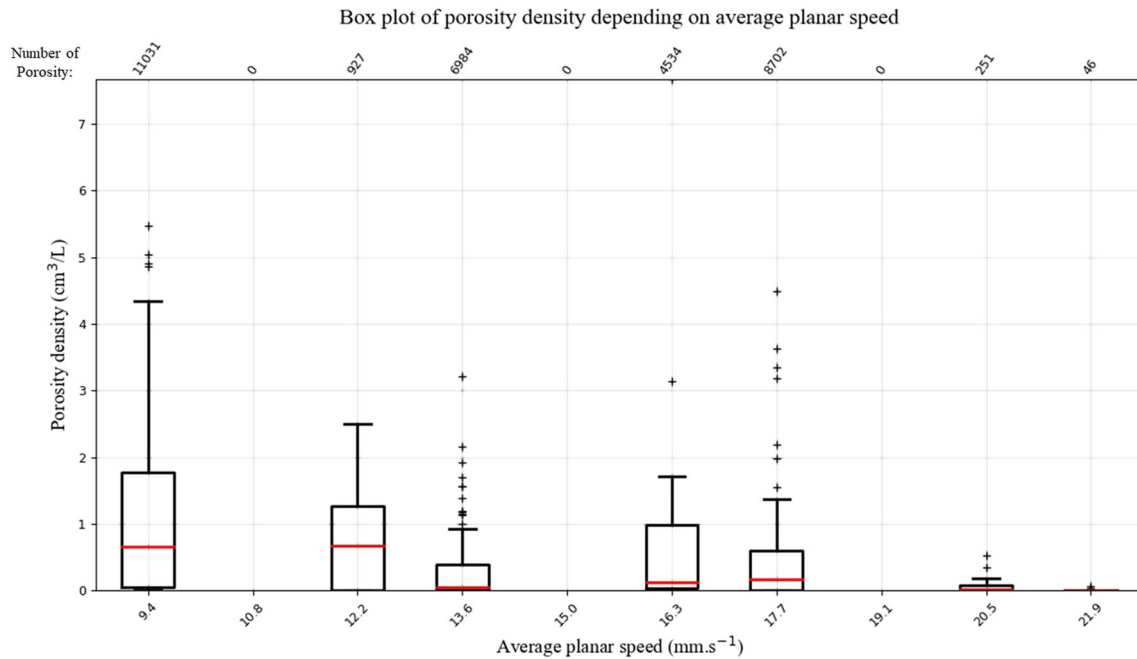
Fig. 11 Porosity versus averaged velocity along the y-direction

the neighborhood on the interface between the part and the substrate. Thus, the dependence of the porosity with respect to the z-coordinate of the computational box was analyzed and the results depicted in Fig. 15, that confirms that porosity increases when the box approaches the substrate.

6. **Layer thickness.**

Figure 16 shows the dependence of the porosity with respect to that parameter, and the porosity increasing for the maximum and minimum values of the layer thickness, very certainly because of the greater difficulty to reach an homogeneous melting when thickness becomes too big or too small.

7. **Turns density.**

Fig. 12 Porosity versus averaged planar velocity

Box plot of porosity density depending on box index along Y
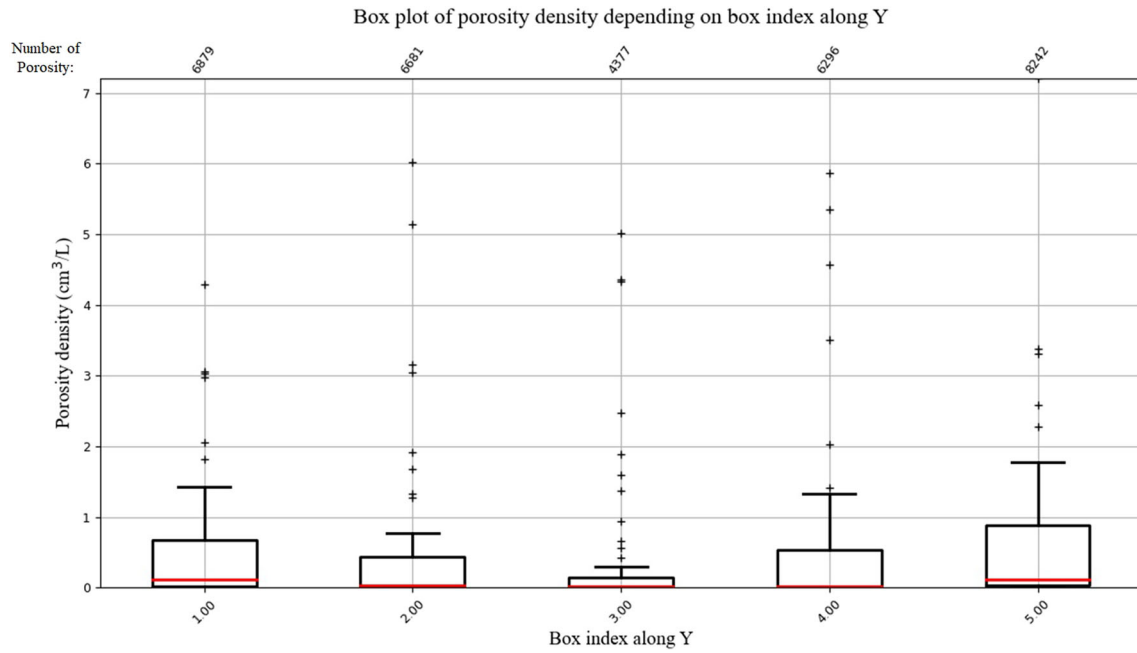
Fig. 13 Porosity versus location of the computational box along the y-direction

When trajectory turns the spatial filling is compromised. It is well known that squares can perfectly cover a surface, however the couverture when using circles remains partial. Here, it is expected that regions where the density of turn is high, this one quantified by the number of turns by unit of volume (cm^3), will exhibit larger porosity. Figure 17 confirms this expectation. Moreover, as the number of turns and the wire diameter (from which the layer thickness depends) are correlated, a similar tendency to the one just discussed is expected.

8. **Laser Power.**

Box plot of porosity density depending on box type
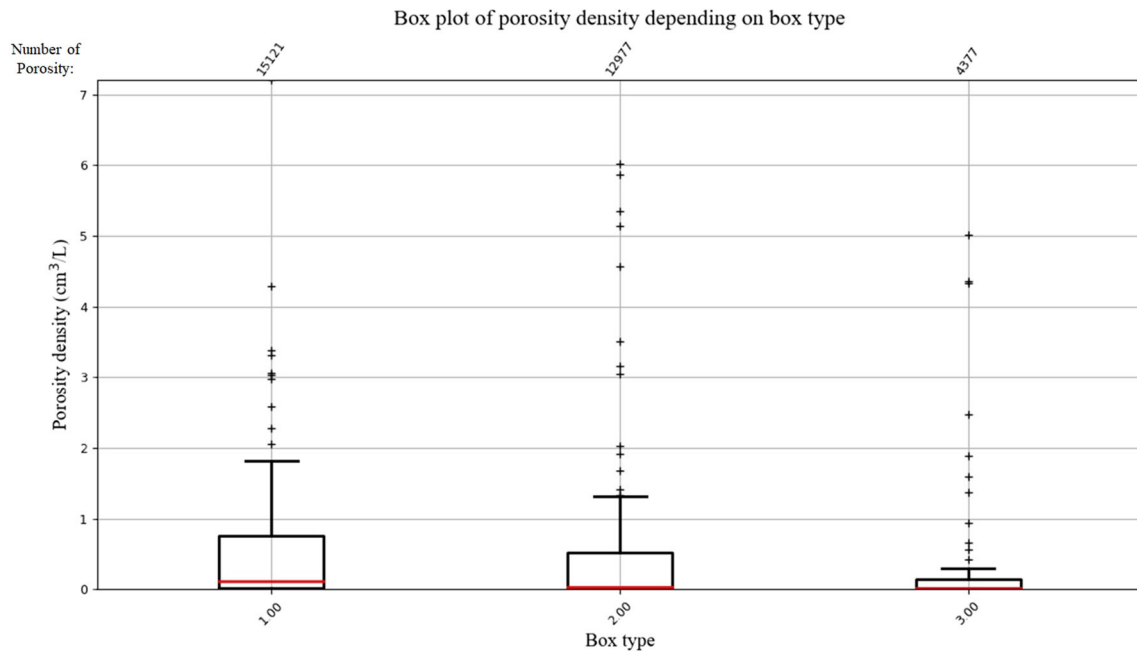
Fig. 14 Porosity versus relative position of the computational bow
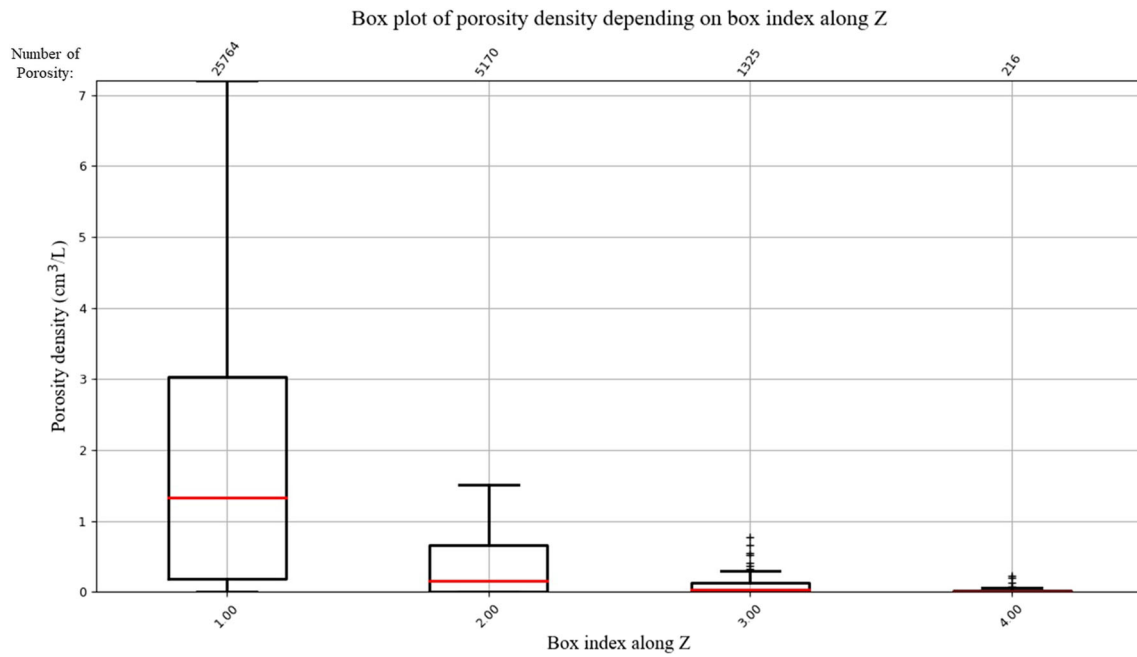
Fig. 15 Porosity with respect to the distance to the substrate (z-coordinate)

The influence of the power, as illustrated in Fig. 18, seems having a less regular behavior, possibly due to the strong couplings and correlation with all the other parameters just discussed. The most physical parameter is the provided heat, and the last depends on the laser power and the velocity.
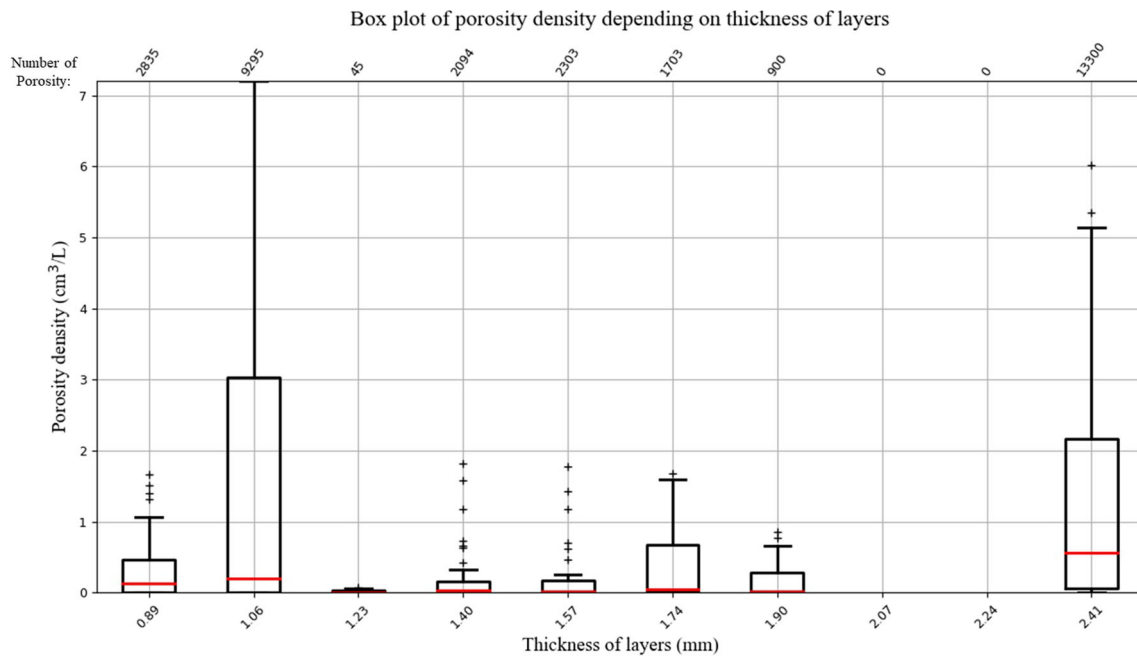
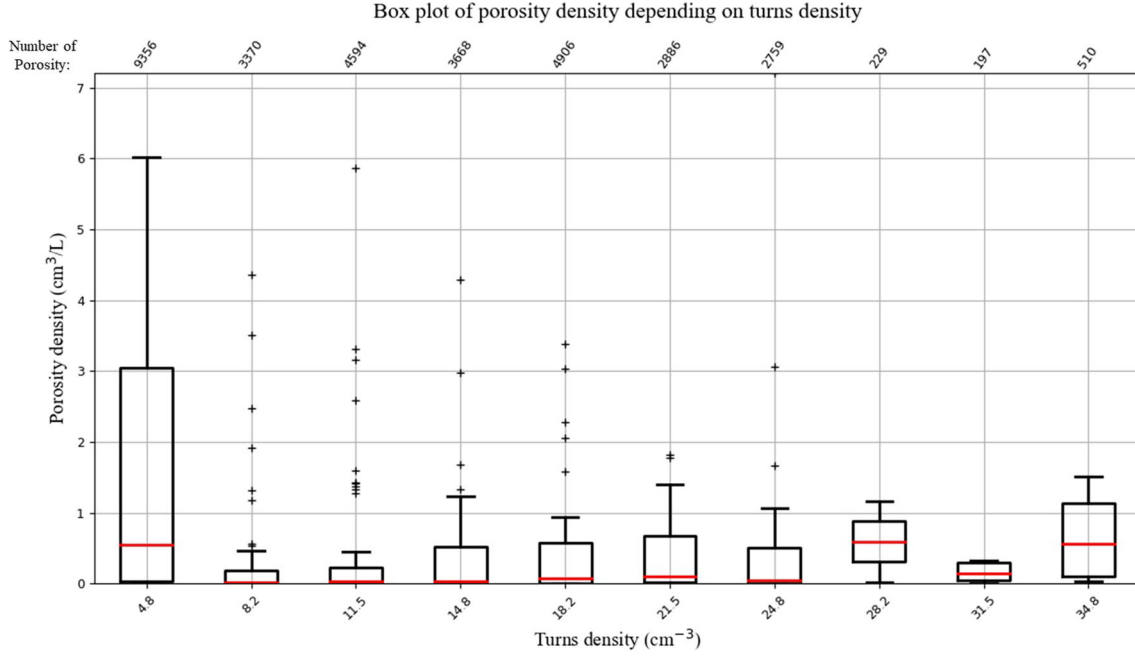**Fig. 16** Porosity versus number layer thickness

Fig. 17 Porosity versus density of trajectory turns

Statistical model

Now, for all the computational boxes N_b (thirteen parts consisting of $1 \times 5 \times 4 = 20$ boxes) the quantity of interest –QoI– Y (the porosity volume fraction), is being related to the process parameters grouped in vector X.

Thus, for each box, $i = 1, ..., N_b$, the parameters vector X^i and the associated QoI, Y^i, are assumed known and

a regression linking both is searched in the generic form $Y = f(X)$, while knowing

$$Y^i = f(X^i), \quad i = 1, ..., N_b. \tag{3}$$

Vector X^i contains all the parameters just introduced and discussed:

$$X^i = \begin{bmatrix} \overline{V}^i_X & \overline{V}^i_Y & \overline{V}^i_{XY} & \eta^i_{layers} & \delta^i_{turns} & i^i_Z & typ^i & \mathbb{P}^i \end{bmatrix}, \tag{4}$$
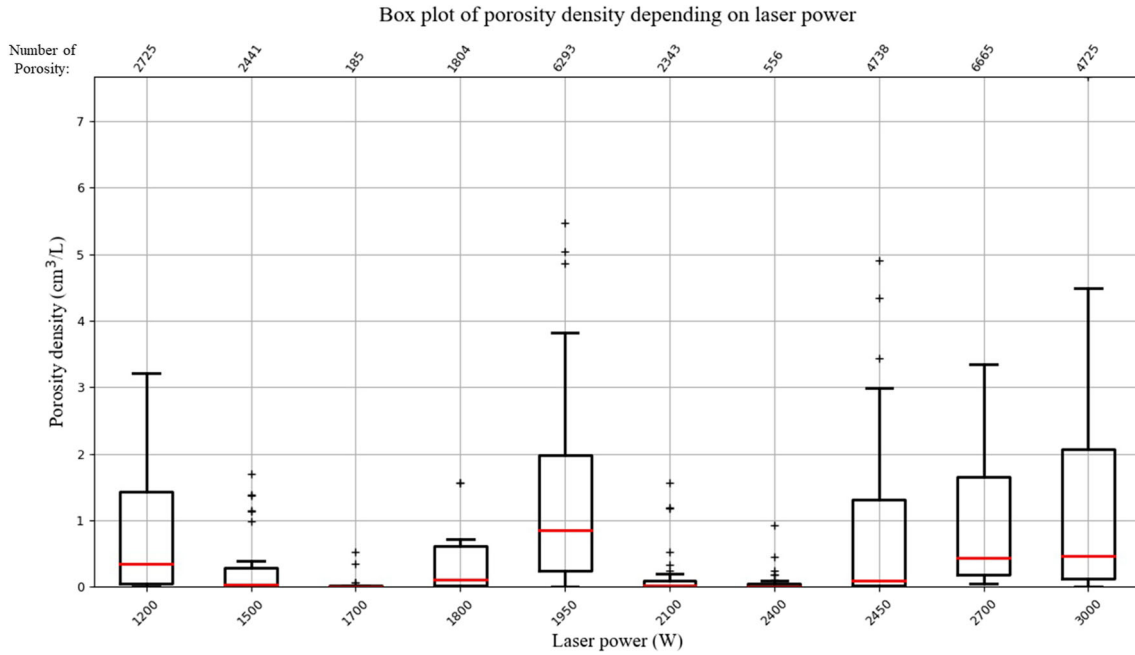

Fig. 18 Porosity versus reference laser power

referring respectively to: the averaged velocity along the x and y-coordinates, the average planar velocity that incorporates the effect of the velocity magnitude, the layer thickness, the turns density, the z-coordinate referring to the distance to the substrate, the box type (peripheral or internal) and the laser power.

It is important to note that the learned models explain the average porosity with respect to the average of the local
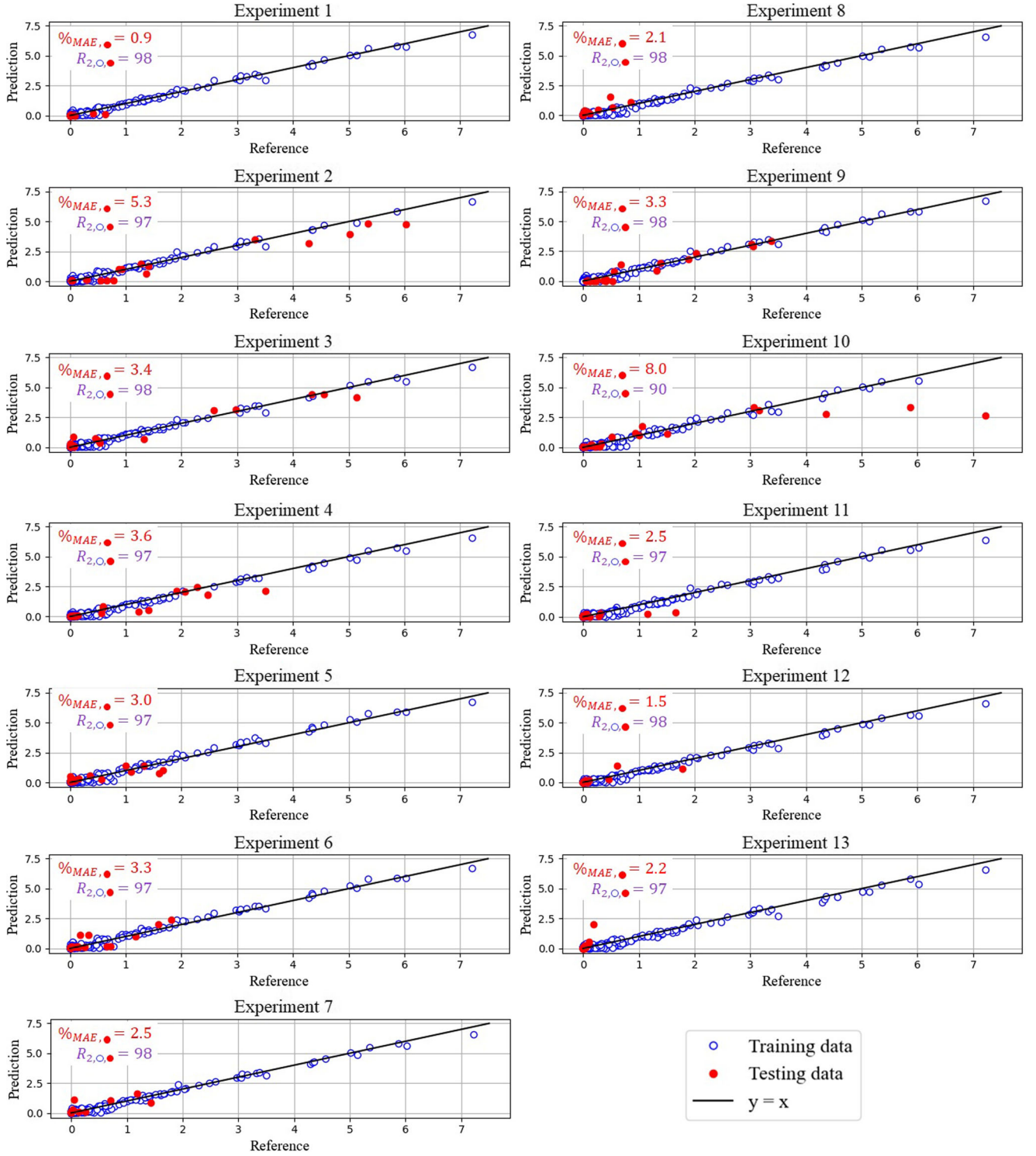
Fig. 19 Reference versus regression predictions. Each subfigure contains 20 red dots, corresponding to the 20 boxes that each experiment contains, even if in some cases it is difficult to appreciate them because of the fact that sometimes different red points are almost superposed

parameters in a box (each part is composed by 20 disjoint boxes). Thus, each experiment provides 20 data that allows covering a large interval of the parameters ensuring the construction of the models.

The regression was constructed by considering all the experiments (printed parts) except one. The remaining part was used for testing the computed regression. The choice of performing such a cross validation was motivated by the reduced amount of experiments, in order to quantify the accuracy and robustness of the proposed procedure.

Neural Network based regression

To evaluate the functional relation expressed by $Y = f(X)$ a Multi-Layer Perceptron –MLP– is considered. There is not novelty concerning the regression choice and its use. To set the MLP hyper-parameters, the algorithm iterated until obtaining results good enough in the approximation function. The MLP is defined by:

– An input and an output layers, respectively constituted of 8 and 1 neurons
– 8 hidden layers consisting of respectively 27, 25, 23, 21, 20, 17 & 36 neurons;
– *Adam* algorithm [27];
– *Relu* activation function: $relu(x) = \max(0, x)$;
– Regularization term $\alpha = 0.5$;
– *The optimization process stops when the score is not improving anymore*, according to the scikit-learn documentation [28].

The implementation was done with the class MLPRegressor available in the scikit-learn package in Python.

The proposed NN seems oversized, however, as discussed later, it was able to ensure accuracy while limiting overfitting. Its size is certainly impacted by the data variability. In all cases, even if the NN is not compact, it is not complex.

Results

Predictions made with the NN-based regression were compared with the existing data, for both, the data in the training and the test sets, blue and red dots respectively. Results are shown in Fig. 19.

The results prove that the training data is well represented while avoiding overfitting, that is, the predictions seem an acceptable compromise between the accuracy obtained in the training and test data-sets. Due to the fact that the available data is not so abundant, we opted for performing a cross validation, whose results are grouped in Fig. 19 where one case is excluded when obtaining the model with the others, and then tested on the one that was excluded. As

it can be seen, the regressions seem general accurate and robust.

It can be noticed that predictions are quite accurate despited the high fluctuations and variability that this process entails. The just referred figure also includes the R_2 score of the regression, which is computed with both the training and the testing data sets, and the $\%_{MAE}$ (defined here to avoid the impact of the negligible values of the porosity):

$$R_2 = 1 - \frac{\sum\limits_{i=1}^{N_b} \left(Y_{ref}^i - Y_{pred}^i\right)^2}{\sum\limits_{i=1}^{N_b} \left(Y_{ref}^i - \overline{Y_{ref}}\right)^2}, \tag{5}$$

$$\%_{MAE} = \frac{100}{N_b} \frac{\sum\limits_{i=1}^{N_b} |Y_{ref}^i - Y_{pred}^i|}{\left|\max(Y_{ref}) - \min(Y_{ref})\right|}, \tag{6}$$

with Y_{ref}^i and Y_{pred}^i respectively the reference and the predicted porosity density of the ith box and $\overline{y_{ref}}$ the mean value of all the true porosity.

In view of the obtained values, the proposed neural network seems quite optimal for the current analysis. Indeed, the R_2 score is always more than 0.90 and the $\%_{MAE}$ percentage is always less than 8%, emphasizing the regression ability for predicting the porosity.

Conclusion

The present paper addressed an alternative modeling approach for predicting the porosity volume fraction in wire laser metal deposition based printed parts. Due to the difficulty of using physics-based models for the reasons discussed in the introduction section, this paper proposed the use of a NN-based nonlinear regression for predicting the amount of porosity as a function of seven local process parameters and the laser power.

First, the parameters to be used in the regression construction were proposed and their effect on the observed and measured porosity analyzed. As soon as the correlation was confirmed, they were retained to be part of the input parameters for the regression. A MLP Neural Network was constructed and trained with a part of the available data. Then, the regression performances were evaluated on both data-sets, the one used in the training and the one reserved to test the prediction capabilities on new process conditions.

The results reported all along this works proved the ability of the selected parameters to explain and predict the observed porosity. Thus, future works will consider the knowledge encapsulated in this regression for better

define the process itself, in order to minimize the amount of porosity, and also for online control purposes.

Declarations

Conflict of Interests The authors declare that they have no conflict of interest.

References

1. Biswal R, Zhang X, Syed AK, Awd M, Ding J, Walther F, Williams S (2019) Criticality of porosity defects on the fatigue performance of wire+ arc additive manufactured titanium alloy. Int J Fatigue 122:208–217

2. Frazier WE (2014) Metal additive manufacturing: A review. Journal of Materials Engineering and Performance 23(6):1917–1928

3. Thompson SM, Bian L, Shamsaei N, Yadollahi A (2015) An overview of direct laser deposition for additive manufacturing; part i: Transport phenomena, modeling and diagnostics. Additive Manufacturing 8:36–62

4. Shamsaei N, Yadollahi A, Bian L, Thompson SM (2015) An overview of direct laser deposition for additive manufacturing; part ii: Mechanical behavior, process parameter optimization and control. Additive Manufacturing 8:12–35

5. Derekar K (2018) A review of wire arc additive manufacturing and advances in wire arc additive manufacturing of aluminium. Mater Sci Technol 34(8):895–916

6. Rodrigues TA, Duarte V, Miranda R, Santos TG, Oliveira J (2019) Current status and perspectives on wire and arc additive manufacturing (waam). Materials 12(7):1121

7. Jiang-zhou S, Mu-zheng X, Zhi-jing Z, Zhi-peng Y, Jin X, Yi-chong Y (2017) Microstructural morphology and evolution of austenite stainless steel deposited with pulsed laser and wire. Int J Adv Manuf Technol 93(9-12):3357–3370

8. Akbari M, Kovacevic R (2018) An investigation on mechanical and microstructural properties of 316lsi parts fabricated by a robotized laser/wire direct metal deposition system. Additive Manufacturing 23:487–497

9. Ge J, Ma T, Chen Y, Jin T, Fu H, Xiao R, Lei Y, Lin J (2019) Wire-arc additive manufacturing h13 part: 3d pore distribution, microstructural evolution, and mechanical performances. J Alloys Compd 783:145–155

10. Hauser T, Reisch RT, Breese PP, Lutz BS, Pantano M, Nalam Y, Bela K, Kamps T, Volpp J, Kaplan AF (2021) Porosity in wire arc additive manufacturing of aluminium alloys, vol 41

11. Brice CA, Schwendner KI, Mahaffey DW, Moore EH, Fraser HL (1999) Process Variable Effects on Laser Deposited Ti-6Al-4V. Solid Freeform Fabrication, pp 369–374. http://utwired.engr.utexas.edu/lff/symposium/proceedingsArchive/pubs/Manuscripts/1999/1999-043-Brice.pdf

12. Zhong C, Gasser A, Schopphoven T, Poprawe R (2015) Experimental study of porosity reduction in high deposition-rate Laser Material Deposition. Optics & Laser Technology 75:87–92. https://doi.org/10.1016/j.optlastec.2015.06.016, https://www.sciencedirect.com/science/article/pii/S0030399215001784

13. Chekir N, Tian Y, Gauvin R, Brodusch N, Sixsmith J, Brochu M (2018) Laser wire deposition of thick ti-6al-4v buildups: Heat transfer model, microstructure, and mechanical properties evaluations. Metall and Mater Trans A 49(12):6490–6508

14. Bock FE, Herrnring J, Froend M, Enz J, Kashaev N, Klusemann B (2021) Experimental and numerical thermo-mechanical analysis of wire-based laser metal deposition of al-mg alloys. J Manuf Process 64:982–995

15. Chiumenti M, Cervera M, Salmi A, De Saracibar CA, Dialami N, Matsui K (2010) Finite element modeling of multi-pass welding and shaped metal deposition processes. Comput Methods Appl Mech Eng 199(37-40):2343–2359

16. Bai X, Colegrove P, Ding J, Zhou X, Diao C, Bridgeman P, roman Hönnige J, Zhang H, Williams S (2018) Numerical analysis of heat transfer and fluid flow in multilayer deposition of paw-based wire and arc additive manufacturing. Int J Heat Mass Transfer 124:504–516

17. Martin AA, Calta NP, Khairallah SA, Wang J, Depond PJ, Fong AY, Thampy V, Guss GM, Kiss AM, Stone KH et al (2019) Dynamics of pore formation during laser powder bed fusion additive manufacturing. Nat Commun 10(1):1–10

18. Arrizubieta JI, Lamikiz A, Cortina M, Ukar E, Alberdi A (2018) Hardness, grainsize and porosity formation prediction on the laser metal deposition of aisi 304 stainless steel. Int J Mach Tools Manuf 135:53–64

19. Ning J, Wang W, Zamorano B, Liang SY (2019) Analytical modeling of lack-of-fusion porosity in metal additive manufacturing. Applied Physics A: Materials Science and Processing 125(11):1–11. https://doi.org/10.1007/s00339-019-3092-9

20. Bayat M, Mohanty S, Hattel JH (2019) Multiphysics modelling of lack-of-fusion voids formation and evolution in IN718 made by multi-track/multi-layer l-PBF. Int J Heat Mass Transfer 139:95–114. https://doi.org/10.1016/j.ijheatmasstransfer.2019.05.003

21. Xia M, Gu D, Yu G, Dai D, Chen H, Shi Q (2017) Porosity evolution and its thermodynamic mechanism of randomly packed powder-bed during selective laser melting of Inconel 718 alloy. International Journal of Machine Tools and Manufacture 116:96–106. https://doi.org/10.1016/j.ijmachtools.2017.01.005, https://www.sciencedirect.com/science/article/pii/S0890695516305387

22. Panwisawas C, Qiu CL, Sovani Y, Brooks JW, Attallah MM, Basoalto HC (2015) On the role of thermal fluid dynamics into the evolution of porosity during selective laser melting. Scripta Materialia 105:14–17. https://doi.org/10.1016/j.scriptamat.2015.04.016, https://www.sciencedirect.com/science/article/pii/S135964621500158X

23. Wang C, Tan X, Tor S, Lim C (2020) Machine learning in additive manufacturing: State-of-the-art and perspectives, Additive Manufacturing, pp 101538

24. Garg A, Lam JSL, Savalani M (2015) A new computational intelligence approach in formulation of functional relationship of open porosity of the additive manufacturing process. Int J Adv Manuf Technol 80(1):555–565

25. Khanzadeh M, Chowdhury S, Tschopp MA, Doude HR, Marufuzzaman M, Bian L (2019) In-situ monitoring of melt

pool images for porosity prediction in directed energy deposition processes. IISE Trans 51(5):437–455

26. Tian Q, Guo S, Guo Y et al (2020) A physics-driven deep learning model for process-porosity causal relationship and porosity prediction with interpretability in laser metal deposition. CIRP Ann 69(1):205–208

27. Kingma DP, Ba J Adam: A method for stochastic optimization, arXiv preprint arXiv:1412.6980

28. Scikit-Learn MLPRegressor—Reference Manual, https://scikit-learn.org/stable/modules/generated/sklearn.neural_network.MLPRegressor.html?highlight=mlpregressor#sklearn.neural_network.MLPRegressor, [Online; accessed 28-May-2021] (2021)